Two-dimensional thermometry measurements in confined swirl flames using filtered Rayleigh scattering

Meng Li[1] · Bo Yan[1] · Li Chen[1] · Shuang Chen[1]

Abstract

Two-dimensional temperature measurements using filtered Rayleigh scattering (FRS) were performed in confined CH_4/air swirl flames at atmospheric pressure. The investigated burner has a combustion chamber consisted of four quartz windows. The combustion chamber is 160 mm high with a square section of 50×50 mm^2. Measurements were challenging due to the strong interference from the incident laser impinging onto quartz windows, wall reflection and Mie scattering. Comparisons between the FRS and a conventional probe-based thermocouple were conducted through several investigated cases. Five operating conditions were studied with the equivalence ratios (Φ) of the premixed CH_4/air mixture covered a range of 0.67–0.83. Under each condition, five cross sections (*C.S.*) of the swirl flame were investigated and compared to analyze (1) the flame structures and temperature distributions of the instantaneous FRS images and (2) the uniform temperature radius as well as the joint probability density function (PDF) profiles of the averaged FRS signals. Results indicate that FRS can effectively suppress the background scattering and the average standard deviation of FRS measurements throughout the experiment is $< 7.5\%$. The thermochemical state of the confined swirl flames is strongly influenced by Φ, leading to varieties of flame structures and temperature distributions.

1 Introduction

Premixed turbulent flames allow for a detailed understanding in fundamental research of increasing the overall efficiency of aero engines and gas turbines, in which flame chemistry is highly coupled with flow turbulence [1, 2]. Turbulent flames are susceptible to thermoacoustic pulsations generated by the combustion mechanism and sustained by a resonant feedback process coupling pressure and heat transfer [3–6]. These instabilities would result in strong perturbations in a combustion field and even destruction of system components. The mechanisms leading to the flow instabilities are based on a complex interaction between burner geometry and significant combustion processes, such as chemical reaction, flow mixing, pressure and heat transfer, which are not well understood yet [7, 8]. Temperature is an essential scalar for evaluating the qualities of combustion processes [9]. While conventional probe-based temperature measurement techniques have been readily available and adequately tested, most of them are point-wise and would perturb the investigation region significantly [2]. To gain deeper insight into the temperature distribution of a turbulent flame, planar optical measurement techniques are needed.

For non-disturbing temperature measurement, laser-based diagnostic techniques are preferred as they can provide high temporal and spatial resolution [10–13]. There are multiple different thermometry approaches, such as laser Rayleigh scattering (LRS) [14–16] and coherent anti-Stokes Raman scattering (CARS) [17, 18]. Between the two thermometry approaches, LRS is specific since it can be used to carry out multi-dimensional temperature measurement, while CARS is limited to point-based measurements. Besides, LRS has qualities of experimental simplicity and high signal-to-noise (SNR). These advantages have made LRS a common approach for planar-based thermometry [19–21]. However, as the Rayleigh scattering belongs to the "quasi-elastic" light

✉ Meng Li
1977410231@qq.com

Bo Yan
372340756@qq.com

Li Chen
chenli_03@163.com

Shuang Chen
chenshuang56@126.com

1   State Key Laboratory of Aerodynamics, China Aerodynamics Research and Development Center, Mianyang 621000, Sichuan, China

scattering, the wavelength of the collected signal is equal to the incident laser wavelength. In such a manner, LRS signal is impressionable to unwanted background scattering interferences including surfaces scattering of wall reflection and Mie scattering of large particles. This limits the range of applications of LRS since it requires large space to avoid surface scattering and clean flow to reduce Mie scattering [22–24].

A solution to this problem persecute LRS is the filtered Rayleigh scattering (FRS) [25–28], which is a modification of the traditional LRS and makes use of the absorption bands of atomic or molecular vapors to remove the unwanted surface/particle scattering from the desired scattering signal. Figure 1 shows the spectral response of a flame reaction zone illuminated by a narrow linewidth light source. The molecular scattering spectrum (black line) consists of the rotational Raman lines, the Cabannes lines and the vibrational Raman lines. The Cabannes scattering includes the Rayleigh-Brillouin scattering (RBS) and part of the rotational Raman scattering [14, 22]. The RBS is the main component scattering while all forms of Raman scattering composing roughly 2.5% of total molecular scattering in air [29]. The surface/particle scattering profile (blue lines) has the same linewidth as the incident laser but has much higher intensity compared to the RBS intensity. Iodine is chosen as the filter since its spectral is broader than the narrow linewidth laser, but narrower than the RBS profile. The spectral signal collected by the detector is a superposition of iodine transmission curve and RBS of the observed volume element [2, 30, 31]. By tuning the incident laser frequency into the blocking range, surface/particle scattering is then absorbed by the iodine filter. Although the iodine filter has the ability to remove unwanted scattering, it absorb part of the RBS signal as
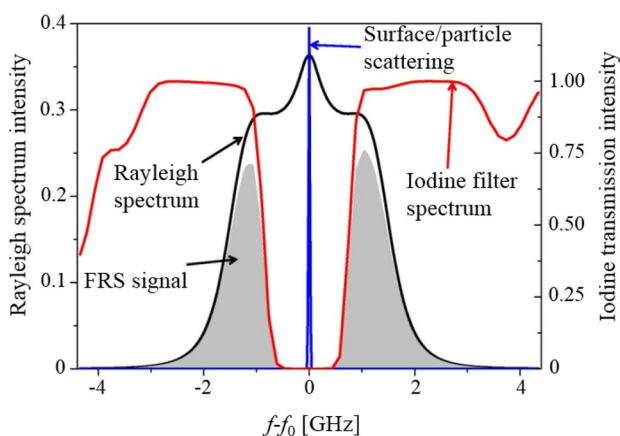

Fig. 1 Scheme of the FRS working principle: the surface/particle scattering (blue line) is absorbed by the I_2 molecular filter (red line), while portion of the FRS signal (gray area) passes through to be collected by the detector

well. So tuning an appropriate filter bandwidth is of great importance for the signal intensity of FRS especially in the kinetic regime.

As discussed previously, the intensity collected by the detector is the convolution of the RBS intensity and the transmission profile of the iodine filter. The RBS spectrum is calculated by Tenti S6 lineshape model [32] since it is considered to be the most utilized and accurate model for diatomic molecules [33]. The measured FRS intensity for each camera pixel element [14, 34] is described by

$$S_{FRS,sf} = cI_0 n \sum_i \varphi_i \Gamma_i, \tag{1}$$

where C represents the efficiency of the collection optics and imaging system, I_0 is the intensity of the incident laser, n is the number density, φ_i is the mole fraction, and Γ_i is a parameter specific to FRS written as

$$\Gamma_i = \left(\frac{\partial \sigma}{\partial \Omega}\right)_i \int_{-\infty}^{\infty} \tau_{I_2}(v) \cdot R_i(P, T, \overrightarrow{V}, \theta; v_{versus}) dv. \tag{2}$$

In the above equation, $(\partial\sigma/\partial\Omega)$ is the Rayleigh scattering cross section, τ_{I_2} is the transmission spectra profile for the iodine filter, R_i is the RBS spectral profile for species i, which is a function of the gas pressure P, gas temperature T, flow velocity $\overrightarrow{V}$, detector collection angle θ, and $v_{versus} = v - v_0 - \triangle v$ is the versus frequency referred to the center laser (incident laser) frequency v_0. Doppler frequency shift $\triangle v$ is related with $\overrightarrow{V}$ and θ.

For methane-fuel premixed flames burning at atmospheric pressure with low fuel velocities ($|\overrightarrow{V}| < 100$ m/s) and low equivalence ratios ($\Phi < 1$), the scattering cross section term in S6 model is nearly constant and the variations of the parameter Γ_i are not large in composition space [21–24, 26, 27, 31]. For this reason, previous researchers computed temperature from FRS signals by means of assuming that the scattering cross section is constant and that the RBS profile function in parameter Γ_i can be determined from N_2 only [17, 26, 27]. Excluding the dependencies on C, I_0, n by dividing Eq. (1) with the referenced FRS measurement of quiescent air at ambient pressure, Eq. (1) can be rewritten to the equation for temperature with respect to the normalized FRS signal intensity parameter $S_{FRS}/S_{FRS,air}$ as

$$T = T_{air} \cdot \frac{S_{FRS,air}}{S_{FRS,sf}} \cdot \frac{\sum_i \varphi_i \Gamma_i}{\Gamma_{N_2}}. \tag{3}$$

Figure 2 shows the relationship between $S_{FRS}/S_{FRS,air}$ and the temperature with the laser wavelength tuned to the iodine transmission notch at 18,787.8 cm^{-1}, based on the RBS spectrum and iodine transmission profile. The
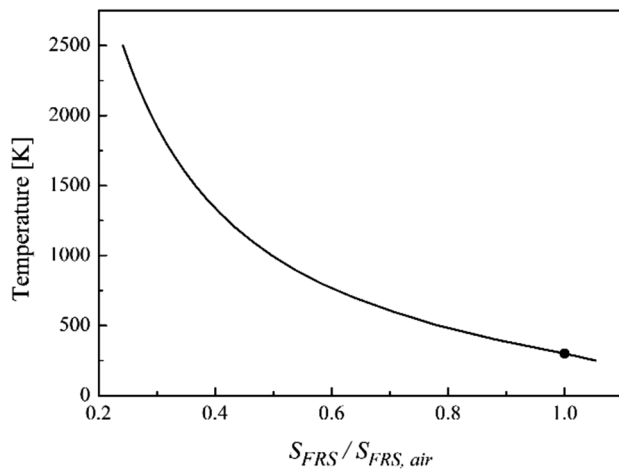
Fig. 2 Scheme of the FRS working principle: the surface/particle scattering (blue line) is absorbed by the I_2 molecular filter (red line), while parts of the FRS signal (black line) pass through

Fig. 3 Experimental setup for FRS temperature measurements in confined swirl flames

normalized FRS signal intensity at the black dot location is equal to 1.0, corresponding to the referenced temperature (299 K, 26 ºC). Therefore, temperature can be deduced from Fig. 2 with the acquisition of the normalized FRS signal from the measurements.

The purpose of this paper is to carry out FRS thermometry in the premixed confined swirl flames at atmospheric pressure generated by a self-designed swirl burner. The burner has a square combustion chamber consists of four quartz windows, which reflect a mass of the incident laser light, leading to strong surface scattering. To demonstrate the efficiency of iodine molecular filtering, a simple experiment was performed to measure the air scattering signal from the combustion chamber with and without the iodine filter. In addition, the equivalence ratios of the premixed CH_4/air mixture covering a range from 0.67 to 0.83 were chosen for the measurements, allowing to study the influence of equivalence Φ on the thermal state of the swirl flames. Comparisons in thermometry measurements between FRS and the thermocouple were made by several investigated cases. The joint probability density functions (PDF) of FRS images were obtained to study the temperature distributions of typical operating conditions.

2 Experimental setup

A general schematic of the experimental setup for this experiment is shown in Fig. 3. The laser source used for the FRS system is an injection-seeded, frequency doubled, Q-switched, Nd: YAG laser operating at 532 nm,
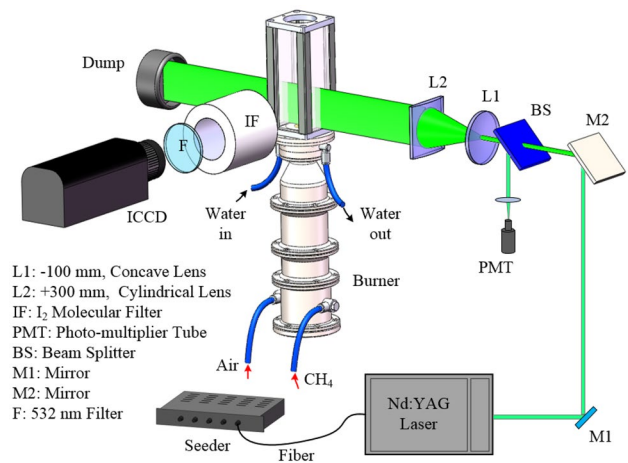
delivered 500 mJ/pulse with a repetition rate of 10 Hz. Before entering the interrogation area, a small portion of the laser beam is extracted using a beam splitter, and routed into a high-resolution photo-multiplier tube (Sens-Teck, P30A-03) to monitor the spectral frequency for each incident laser pulse. Afterwards, the laser beam is broaden by a concave lens with a focal length of − 100 mm then is formed into a light sheet by means of a 300 mm-focal-length cylindrical lens. Finally, the laser sheet illuminates the investigated area and was aligned as it propagates parallel to the surface through the centerline of the burner nozzle. The laser sheet was approximately 0.5 mm thick (FWHM) with a height of 30 mm. The burner consists of a 248-mm-long circular bluff body for fuel and air mixing and a combustion chamber composed of quartz windows with thickness 10 mm held by copper posts in the corners. The combustion chamber has a square section of 50×50 mm^2 and is 160 mm high. The dual-annular nozzle consists of a central rod of diameter 6 mm located along the nozzle axis and a coaxial fuel nozzle (14 mm in diameter) surrounded the rod. The swirl generator inside the nozzle has a swirl number of 0.884. The exit surface of the central nozzle was defined as $h = 0$ for all measurements.

The scattered signal of the investigated section is firstly collected by the self-designed molecular filter, which is a 280-mm-long and 70 mm in diameter glass cylinder, wrapped in electrical resistance heating tape with the side-arm surrounded in a thermal shroud. Then the filtered signal enters a bandpass filter with 1 nm FWHM and finally is focused onto the imaging chip of the ICCD camera. The camera has a maximum resolution of 512×2048 pixel elements with a pixel size of 8.2×8.2 μm^2. It was designed for

Table 1 Investigated flames: Φ is the equivalence ratio

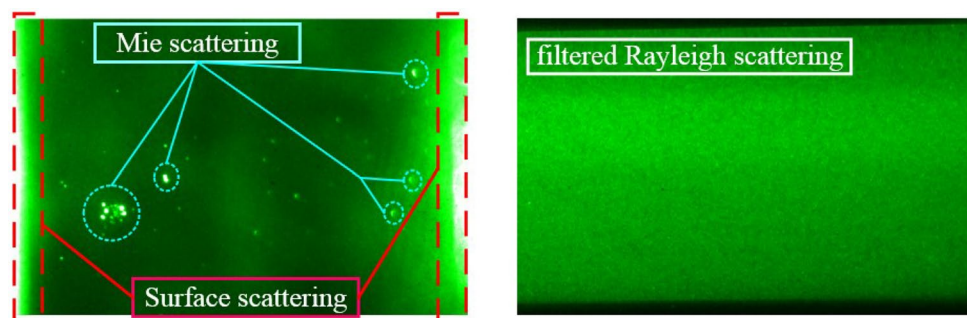| Case	CH$_4$ L/min	Air L/min	Φ	Distances from the central cross sections (mm)				
				$C.S. -10$	$C.S. -5$	$C.S.\ 0$	$C.S.\ 5$	$C.S.\ 10$
1	2.8	40	0.67	-10	-5	0	5	10
2	3.0	40	0.71	-10	-5	0	5	10
3	3.2	40	0.76	-10	-5	0	5	10
4	3.3	40	0.79	-10	-5	0	5	10
5	3.5	40	0.83	-10	-5	0	5	10

Note. Flow rates in standard liters per minute (L/min) are referenced to 1.013 bar and 273 K

signal acquisition under test rig conditions, with the emphasis on stability and flexibility. Temperature fields comprising 450×500 pixel elements (37×41 mm) were measured with a resolution of 0.08 mm throughout the experiment.

The air and fuel flows were controlled by electronic mass flow controllers. Flow rates for different investigated cases are given in Table 1. The equivalence ratio was calculated from the flow rates of Air and CH$_4$. Five cross sections were placed parallel to each other and $C.S.\ 0$ was the central cross section, overlapped with the surface through the axis of the burner nozzle. The positive and negative cross sections covered the entire flame region. The negative signs represented the direction towards the ICCD camera.

To demonstrate the efficiency of the iodine molecular filter for background scattering rejection, scattering image for the non-reacting flow captured with and without the iodine filter was performed. As shown in Fig. 4, without using the iodine filter for the FRS system, the bright primary surface scattering of incident laser impinging onto the quartz windows and Mie scattering from large particles inside the laser sheet can be clearly seen in the scattering image, while the Rayleigh scattering signal form the gas molecules are not visible. Using the iodine filter and tuning the frequency of the incident laser into the absorption band of the iodine molecular filter, the strong background scattering are rejected by the filter, and the Rayleigh scattering light becomes visible.

3 Results and discussion

3.1 Comparison of temperature measurements between FRS and the thermocouple

Before describing the temperature measurement results, one thing needs to be noted is that the thermocouple (Omega, HH806AU) we used in this manuscript. It has been applied for the temperature measurements on a McKenna burner [35]. In that research, the overall thermometry discrepancy between FRS and the thermocouple was lower than 6%, which validated the temperature capability of the two techniques in CH$_4$/air laminar flames.

Figure 5 shows the comparison of temperature measurements between FRS and the thermocouple at $C.S. -5$, $C.S.\ 0$, and $C.S.\ 5$. For each cross section, flames at equivalence ratios between $\Phi = 0.67$ and 0.81 were investigated. Typically, 50 laser shots were captured for the average temperature. Figure 5a shows the experimental arrangement for FRS and thermocouple measurements. The lifted light blue V region represents the chemiluminescence structure of the swirl flame at $C.S.\ 0$. The thermocouple probe was placed at the same location for all measurements. Portion of the thermocouple probe placed inside the flame consisted of 20×20 pixel elements.

Figure 5b–d show the temperature measurements from two techniques. The red I-type symbols represent the standard deviation of FRS temperature results. The red dots conjoined with them are the averaged FRS results and the
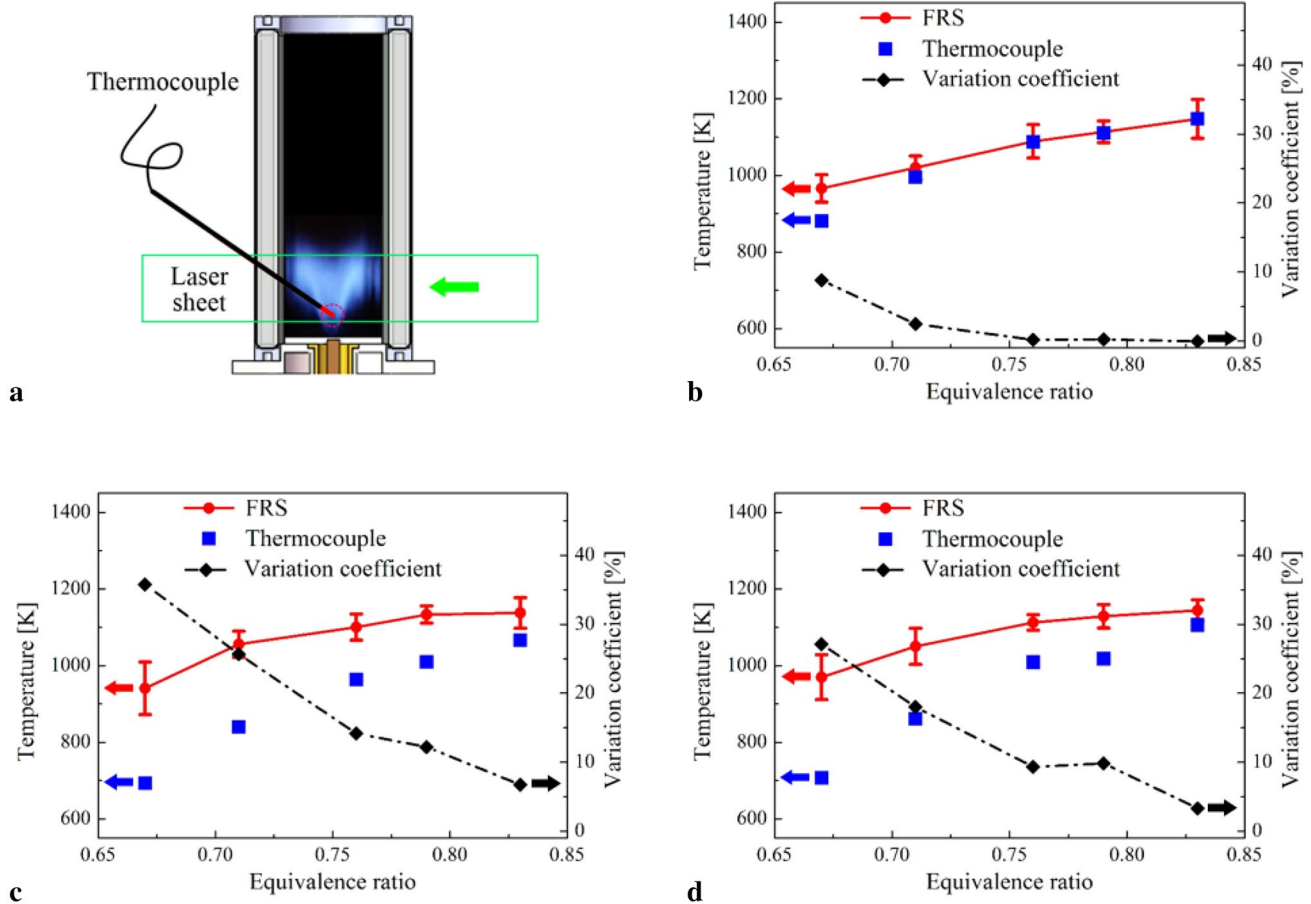
Fig. 4 Comparison of scattering image captured without (left) and with (right) the iodine molecular filter. The background scattering including Mie scattering (blue circled regions) and surface scattering (red boxed regions)

Fig. 5 a FRS thermometry setup and comparison of the temperature measurements between the thermocouple and FRS at three cross sections: **b** *C.S.* 0, **c** *C.S.* − 5 and **d** *C.S.* 5

variation coefficients of the relatively uncertainty between FRS and thermocouple are described by the black diamonds. As can be seen in Fig. 5b, the variation coefficient shows a good agreement lower than 2.5% when equivalence ratio $\Phi > 0.73$. The result validates the thermometry ability of FRS and the thermocouple. However, severe discrepancy occurs at *C.S.* − 5 and *C.S.* 5, in where the flow field changes violently due to strong turbulence. And the thermocouple cannot provide a quick response for the rapid temperature variation. Another unpleasant temperature measurement result from thermocouple is that temperature in *C.S.* 5 are higher than that in *C.S.* − 5, but much lower than that in *C.S.* 0 with maximum deviation of 174 K. This is contrary to actual situation because temperature intensities in *C.S.* − 5 and *C.S.* 5 are supposed to be the same. More importantly, temperature in *C.S.* − 5, *C.S.* 0 and *C.S.* 5 should not vary much because three cross sections are all located in the central high-temperature region of the flame. This indicates that the thermocouple thermometry on swirl flames is not reliable. On the contrary, temperature distributions at *C.S.* − 5, *C.S.* 0 and *C.S.* 5 measured by FRS have a quite similar

appearance. Besides, the mean standard deviations of FRS measurements throughout the experiment is lower than 4%. These evidences demonstrate the ability of FRS thermometry in confined swirl flames.

3.2 FRS thermometry measurements

Figure 6 shows a series of instantaneous temperature images of five flame topologies measured under the case 1–5 conditions (seen in Table 1). The effect of the equivalence ratio Φ on the global flame is showcased in five investigated cross sections *C.S.* − 10, *C.S.* − 5, *C.S.* 0, *C.S.* 5 and *C.S.* 10. The locations of the cross sections and the image sizes are given in mm. It should be noted that a simple algorithm was taken to procedurally identify and eliminate the possible particle scattering in the FRS images. It relies on a signal threshold value that exceeds the known dynamic range of the referenced FRS signals, corresponding to 110% of the peak FRS signal measured in particle-free air. The pixels locations that surpass the threshold as well as its surrounding pixels within
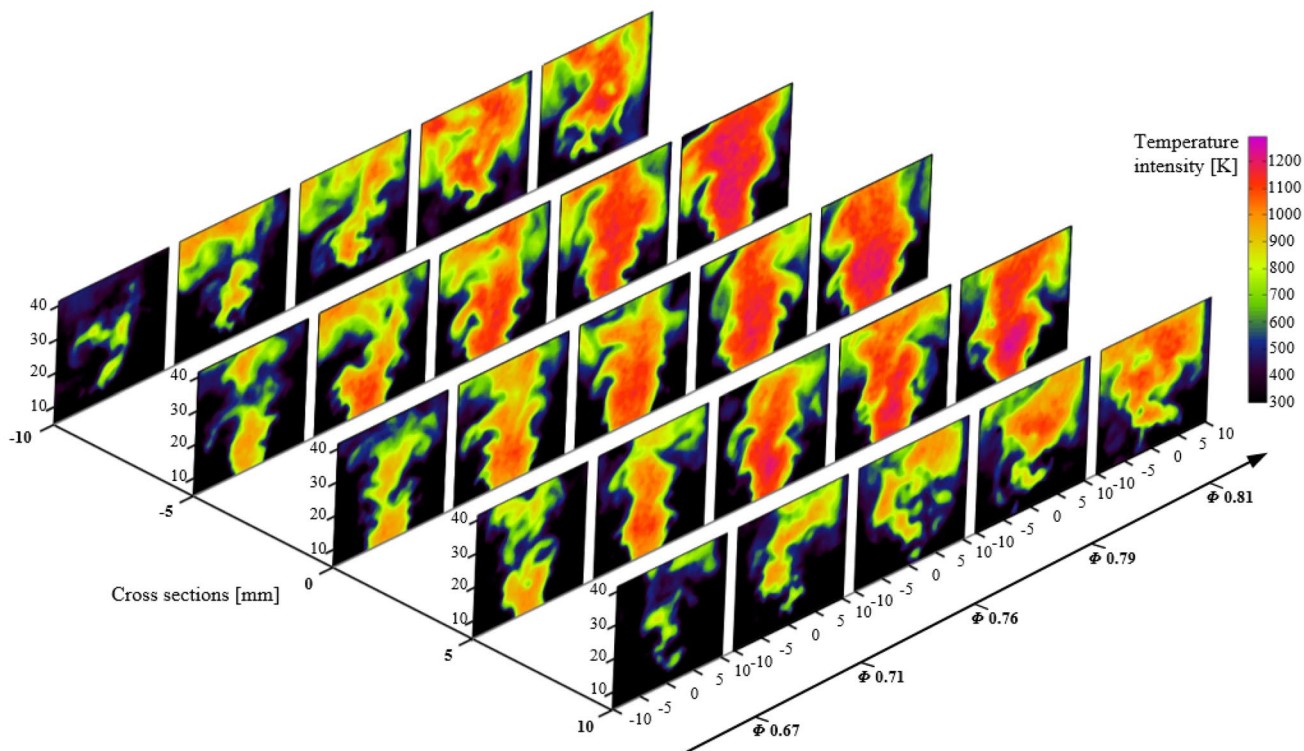
Fig. 6 Instantaneous two-dimensional FRS temperature measurements under case 1–5 conditions

5-pixel radius are set to NaN, and the temperature values will not be computed for those pixel locations.

The instantaneous FRS images in Fig. 6 indicate that the global flame varies strongly in structure and temperature intensity under different Φ conditions. On the edge of the swirl flames, there are lots of vortices rolling on, leading to variously unsteady flame structures. These vortices are mainly aroused by (1) the helical flow instability mechanism, normally recognized as a processing vortex core (PVC) and (2) thermoacoustic oscillations, arising from the interaction between acoustic field and unsteady heat release [36]. PVC describes the process of the vortices from generation in the

shear layer of the burner flow, to breakdown and extrication from the flame [8, 37–39]. The vortices breakdown phenomenon comprises an abrupt change of flame structure at some regions with strong turbulence, which can be seen from the instantaneous images in Fig. 6. Flame structures at low equivalence ratios and in cross sections farther from *C.S.* 0, are more likely torn apart by the vigorous turbulence. To further analyze the effect of the equivalence ratio on the flame features, representatively are, flame structure and temperature distribution, two typical measurements were performed to acquire the average flame images (1) in five cross sections with an equivalence ratio $\Phi = 0.83$ (related to case
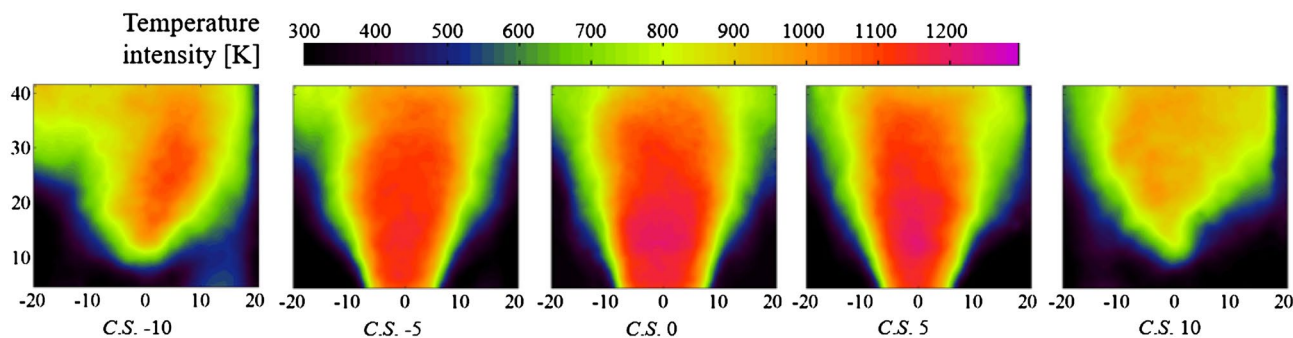

Fig. 7 The average temperature distributions resulting from 50 instantaneous images at 5 cross sections with an equivalence ratio $\Phi = 0.83$

1 in Table 1) and (2) under five Φ conditions in the central cross section (*C.S.* 0).

Figure 7 displays the average temperature distributions in five cross sections with an equivalence ratio $\Phi = 0.83$. A number of 50 single-shot measurements at each cross section is used to obtain the mean value. One obvious feature is that the temperature intensity decreases with the investigated cross section moving away from the central cross section. Though the global flame has an axisymmetric structure, there are deviations in opposed cross sections. For instance, in comparison to *C.S.* 10, and temperature intensity in *C.S.* -10 is much higher and the flame structure is distinctly different. A further point should be noted is that a hot region connected with the main flame locates at the bottom right corner of the *C.S.* -10 image. This region has a maximum temperature of 560 K and will not be explained by the FRS measurement uncertainty. Since both cross sections go through the outer recirculation zone (orz) and flame shear layer zone, these deviations are possible to appear due to strong turbulence in these regions.

Statistical analysis for the images in Fig. 7 are displayed in Fig. 8. The boundary curves extracted from the five flame structures is shown in Fig. 8a. The horizontal axis represents the quantified uniform temperature radius, which is defined as the horizontal distance between the nozzle axis and the outermost pixels with the intensity equal to 450 K. All the curves eventually terminate at a maximum uniform temperature radius of 20.3 mm. It can be clearly observed that there are some wrinkles exist in the boundary curves, especially at the cross sections farther from *C.S.* 0. This is corresponding to the diverse flame structures in the instantaneous images aroused by

the strong flow turbulence. The joint probability density function (PDF) profiles corresponding the average FRS images in Fig. 7 enables the quantification of the temperature distributions at different cross sections, as is seen in Fig. 8b. The orz manifests itself in each PDF profiles at a temperature around 320 K. The temperature of orz is greater than 300 K because of the heat transfer from the flame zone. The second peak around 460 K corresponds to the flame boundary zone of the main flame in different cross sections. No evident difference occurs between the opposed cross sections until the temperature reaches a value great than 820 K, containing the third peak related to the central high-temperature zone of the flame. Apparently, the hot region in *C.S.* -10 is in the temperature range little higher than that in *C.S.* 10. This is in consensus with the observations from Fig. 7. Together with conclusions acquired from Figs. 7, 8 explains the characteristic symmetric structure of the swirl flame.

The average temperature distribution images in *C.S.* 0 under five Φ conditions, are presented in Fig. 9. For the mean structure resulting from 50 instantaneous images, vortices exhibited in the instantaneous images are almost invisible. The flame structures shows good symmetry with respect to the central nozzle axis. For this reason, the uniform temperature radius are extracted only from the left side of the average flame axis. Detailed statistical analysis for the uniform temperature radius and PDF profile of Fig. 9 are shown in Fig. 10. It is clearly seen that the uniform temperature radius and temperature intensity increase with the increasing of equivalence ratio Φ. Coincidently, the five PDF profiles in Fig. 10b have one intersection around temperature $= 700$ K, which is somewhere in between the central
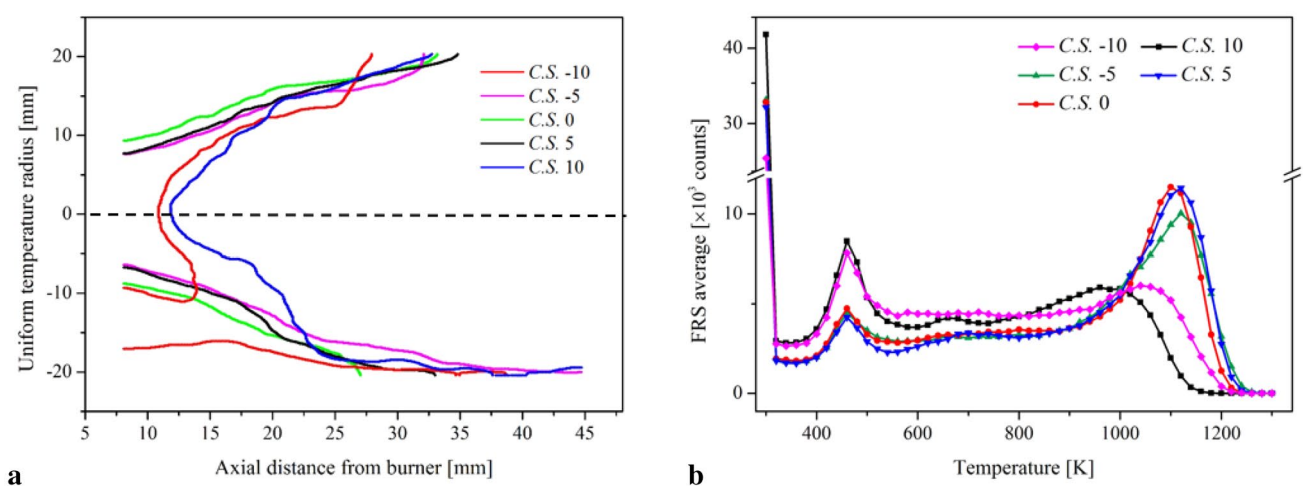

a

b

Fig. 8 Statistical analysis for the average temperature distributions resulting from 50 instantaneous images at 5 cross sections with an equivalence ratio $\Phi = 0.83$. **a** The boundary curves of the average FRS images: the horizontal axis represents the quantified uniform temperature radius and the vertical axis is the distance above the burner surface. **b** The joint probability density function (PDF) profiles corresponding to the average FRS images
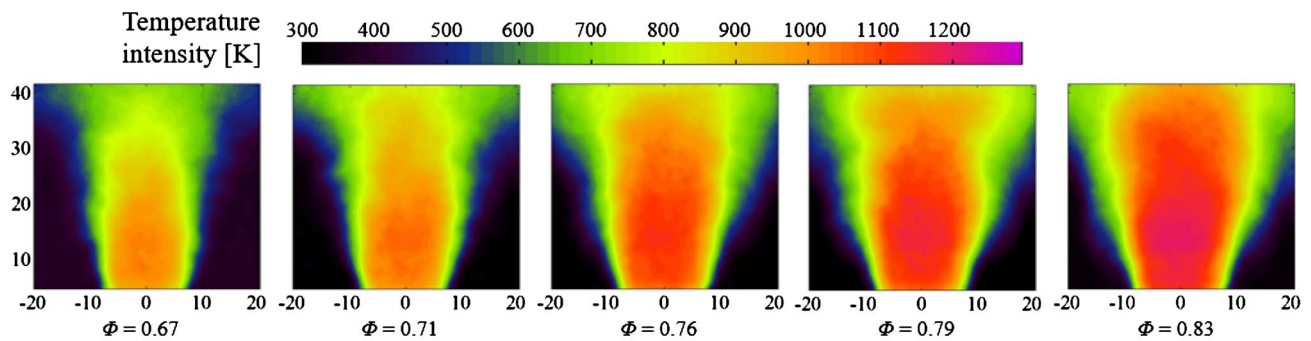
Fig. 9 The average temperature distributions resulting from 50 instantaneous images under different Φ conditions at C.S. 0
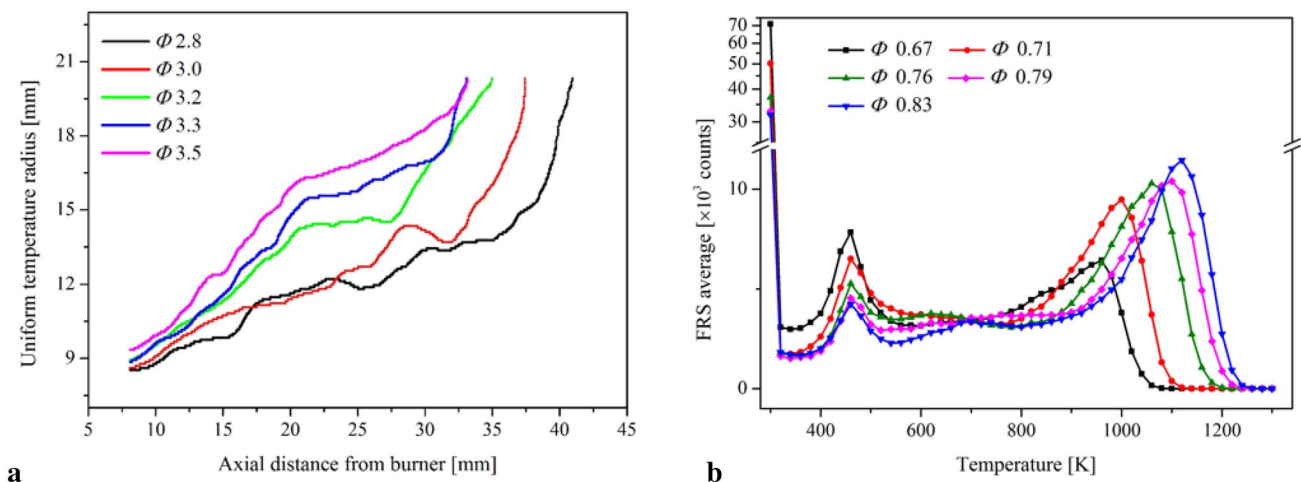

Fig. 10 Statistical analysis for the average temperature distributions resulting from 50 instantaneous images under different Φ conditions at *C.S.* 0. **a** The relationship between the quantified uniform temperature radius and the distance above the burner surface. **b** The joint probability density function (PDF) profiles corresponding to the average FRS images

high-temperature region and low-temperature border of the flame.

4 Summary

FRS were used to obtain two-dimensional temperature distributions of confined premixed swirl CH$_4$/air flames at atmospheric pressure. Five operating conditions were investigated in this experiment (equivalence ratio Φ between 0.67 and 0.83). Under each Φ condition, five cross sections of the swirl flame were chosen for flame structure and temperature measurements. The locations of the five cross sections covered a range from − 10 to 10 mm. Comparisons between FRS and the thermocouple were carried out by temperature measurements in *C.S.* − 5, *C.S.* 0 and *C.S.* 5. The average standard deviation of FRS measurements was < 7.5%. It also turned out that the thermocouple thermometry on swirl flames was inapplicable because of its long-time response against the fast changing flow structure due to strong turbulence.

For the characterizations of the swirl flames, instantaneous and average FRS measurements were performed. Variations between the instantaneous images demonstrated that flow turbulence had significantly influence on flow structure. The joint probability density function profiles related to the temperature distributions were extracted from the average FRS images. The PDF profiles indicated that the flow field could be divided into three different regimes: an outer recirculation zone, a flame boundary zone and a central high-temperature zone. The thermochemical state of the flames was strongly influenced by equivalence ratio Φ, which determined the level of reaction process in the flame region, leading to various temperature distributions and structures of the flames. Significant differences were observed between the opposed cross sections, due to strong turbulence in the flow field.

The key weakness of FRS is the sampling rate of its imaging system, which makes identification of flame structures challenging. This weakness, however, can be less important as higher pulse-energy and sampling rate laser technology becomes available.

References

1. S.B. Pope, Annu. Rev. Fluid Mech. **19**, 237 (1987)
2. U. Doll, M. Fischer, G. Stockhausen, C.E. Willert, Frequency scanning filtered Rayleigh scattering in combustion experiments. In:16th Int Symp on applications of laser techniques to fluid mechanics, 9–12 July, (Lisbon, Portugal, 2012)
3. J.J. Keller, AIAA J. **33**, 2280 (1995)
4. C.O. Paschereit, E. Gutmark, W. Weisenstein, Combust. Sci. Technol. **138**, 213 (1998)
5. S. Candel, P. Combust. Inst. **29**, 1 (2002)
6. J.G. Lee, D.A. Santavicca, J. Propul. Power **19**, 735 (2003)
7. N. Syred, Prog. Energy Combust. Sci. **32**, 93 (2006)
8. W. Meter, P. Weigand, X.R. Duan, R. Giezendanne-Thoben, Combust. Flame **150**, 2 (2007)
9. I.T. Monje, J.A. Sutton, *AIAA Aerospace Science Meeting, 8–12 January* (Kissimmee, Florida, 2018).
10. A.C. Eckbreth, *Laser Diagnostics for Combustion Temperature and Species* (Gordon and Breach Publishers, Amsterdam, 1996).
11. R.P. Lucht, Combust. Flame **133**, 507 (2002)
12. K. Kohse-Höinghaus, R.S. Barlow, M. Aldén, J. Wolfrum, Proc. Combust. Inst. **30**, 89 (2005)
13. R.S. Barlow, Proc. Combust. Inst. **31**, 49 (2007)
14. R. Pitz, R. Cattolica, F. Robben, L. Talbot, Combust. Flame **27**, 313 (1976)
15. J.A. Lock, R.G. Seasholtz, W.T. John, Appl. Optics **31**, 2839 (1992)
16. J. Panda, R.G. Seasholtz, AIAA J. **99**, 0296 (1999)
17. D.A. Greenhalgh, *Quantitative CARS Spectroscopy* (Advances in Non-linear Spectroscopy, New York, 1988).
18. E.D. Fouad, Vib. Spectrosc. **55**, 1 (2011)
19. R.W. Dibble, R.E. Hollenbach, Laser Rayleigh thermometry in turbulent flames. Symp. (Int.) Combust. **18**, 1489 (1981)
20. F.C. Gouldin, R.N. Halthore, Exp. Fluids **4**, 269 (1996)
21. R.B. Miles, W.R. Lempert, J.N. Forkey, Meas. Sci. Technol. **12**, 33 (2001)
22. D. Hofmann, A. Leipert, Temperature field measurements in a sooting flame by filtered Rayleigh scattering (FRS). Symp. (Int.) Combust. **26**, 945 (1996)
23. G.S. Elliott, N. Glumac, C.D. Carter, A.S. Nejad, Combust. Sci. Technol. **125**, 351 (1997)
24. G.S. Elliott, N. Glumac, C.D. Carter, *37th AIAA Aerospace Sciences Meeting and Exhibit, 11–14 January* (Reno, Nevada, 1999).
25. A.P. Yalin, R.B. Miles, Thermophys. Heat Transf. **14**, 210 (2000)
26. G.S. Elliott, N. Glumac, C.D. Carter, Meas. Sci. Technol. **12**, 45 (2001)
27. D. Most, A. Leipertz, Appl. Opt. **30**, 5379 (2001)
28. M. Boguszko, G.S. Elliott, Prog. Aerosp. Sci. **41**, 93 (2005)
29. F. David, B.M. Goldberg, M.N. Shneider, R.B. Miles, AIAA J. **57**, 5067 (2019)
30. T.A. McManus, I.T. Monje, J.A. Sutton, APPL. PHYS. B-LASERS O. **125**, 13 (2019)
31. T.A. McManus, J.A. Sutton, Exp. Fluids **61**, 134 (2020)
32. G. Tenti, C. Boley, R. Desai, Can. J. Phys. **52**, 285 (1974)
33. A.T. Young, G.W. Kattawar, Appl. Optics **22**, 3668 (1983)
34. J. Forkey: Development and demonstration of filtered Rayleigh scattering: a laser based flow diagnostic for planar measurement of velocity, temperature and pressure (PhD thesis, Princeton University 1996)
35. B. Yan, L. Chen, M. Li, S. Chen, C. Gong, F.R. Yang, Y.G. Wu, J.N. Zhou, J.H. Mu, Chin. Phys. B **29**, 024701 (2020)
36. J.P. Moeck, J.F. Bourgouin, D. Durox, T. Schuller, S. Candel, Combust. Flame **159**, 2650 (2012)
37. R. Sadanandan, P. Kutne, A. Steinberg, W. Meier, Flow Turbul. Combust. **89**, 275 (2012)
38. K. Harvey, J. Fluid Mech. **14**, 585 (1962)
39. T.B. Benjamin, J. Fluid Mech. **28**, 65 (1967)